Sol-Gel Derived Cobalt-Doped CeO₂ Nanocomposite on Gold Electrode for Glucose Electrochemical Sensing

N.H. Bansod[1,*,iD], G.N. Chaudhari[1,iD], A.B. Bodade[1,iD] and Prashant B. Kharat[2,iD]

[1]Department of Chemistry, Shri Shivaji Science College, Amravati-444603, India
[2]Department of Physics, Vinayak Vidnyan Mahavidyalaya, Nandgaon Khandeshwar, Amravati-444708, India

*Corresponding author: E-mail: nbansod15@gmail.com

Development of a highly sensitive, repeatable glucose biosensor based on Co-doped CeO₂ nanoparticles is presented in this study. The sol-gel citrate approach was used to synthesize cobalt doped CeO₂ ($Co_xCe_{1-x}O_2$) nanoparticles (5, 10 and 15%). The X-ray diffraction (XRD), UV-visible spectroscopy, FTIR, scanning electron microscopy (SEM) and transmission electron microscopy (TEM) were applied to characterize the structure and morphology of the nanocrystal. The Co-doped CeO₂ nanoparticles-chitosan (CS) composite film was coated on an gold plate using a spin coating process. An adsorption approach created a GOX/CHIT/CCO/Au bioelectrode by immobilizing the enzyme glucose oxidase. The cyclic voltammetry and electrochemical impedance spectroscopy were used to check the electrochemical performance of biosensors. The designed biosensor had an outstanding linear response to glucose oxidase (30–220 mM) by a detection limit of 30 mM. The biosensor has an enormous affinity (K_m = 3.010 mM), excellent repeatability and storage stability up to 28 days.

Keywords: Cerium nanostructure, Sol-gel method, Biosensor.

INTRODUCTION

In recent decade, the metal and metal oxide nanoparticles have emerged as a new topic of nanoscience and technology. The size and shape of nanomaterials have a meaningful impact on their physical, chemical, electrical, optical and surface characteristics [1]. Cerium dioxide, also known as ceria, is the best significant rare-earth oxides in recent years because it has a number of interesting properties, like large specific surface areas, extraordinary electrical conductivity and adequate electron mobility. Each cerium site is bounded by eight oxygen ions inside an face-centered cubic (FCC) structure.

Transition metal-doped ceria nanocrystals have been extensively used to enhance the active oxygen relaxed on the surface of ceric oxide nanoparticles (CeO₂ NPs) by modifying the surface element composition since such materials eventually high catalytic activity [2-5]. Chemical doping of the CeO₂ matrix with suitable dopants (B or In) at the Ce^{4+} site is very efficient for chemo-biosensing applications [6]. The additional active components stabilize the CeO₂ surface and promote grain size reduction, resulting in more significant catalytic activity and sensor responsiveness than pure CeO₂.

In the same situation, Cu–CeO₂ is stronger over Ni and Co-doped CeO₂ catalysts for CO oxidation. Wu *et al.* [7] showed indisputably that CeO₂-supported Cu catalysts exhibit low-temperature activity due to excess Cu^+ and Cu^{2+} concentrations, as well as the relative population of Ce^{3+} and O^- vacancy sites at the surface. Recent attempts have been devoted to improving the thermal and electrical properties of TiO₂ by adding CeO₂. These new materials have been used to make static counter electrodes and sensors. Copper and oxygen that aren't used in a chemical reaction were also developed to increase chemical reactivity and increase oxygen vacancies [8]. Another thing that Co–CeO₂ and Ni–CeO₂ catalysts are better at steam reforming than CO oxidation.

Several studies revealed that the magnetic properties such as ferromagnetism in Co-doped CeO₂ depend mainly on the transition element doping percentage and the structure of a film, including crystalline structure, defects, vacancies, *etc*. Vodungbo *et al.* [9] reported the magnetism in Co-doped CeO₂ layers generated *via* PLD over SrTiO₃ and Si substrates. These thin films exhibited ferromagnetically and had a temper-ature coefficient (TC) greater than 400 K. For example, CeO₂ can

be used to make electrolytes for solid oxide fuel cells, UV blocking components, and chemical mechanical polishing. It can also be used to produce oxygen gas detectors. Several types of organic matrix polysaccharides, collagen and amino acids were utilized as templates [10-12].

Chitosan is a crucial template in the biomineralization process [13-15]. It is also used for biosensors, adsorbents, drug delivery, wound dressing, and antibacterial purposes because it is non-toxic and safe for humans [16]. Chitosan is a biomolecule that has both hydroxyl and amino groups. It can change the shape and crystal phase of the mineral formed during biomineralization [17]. With expectation, the functions of cerium oxide and chitosan will be combined. Nanocomposite Co-doped CeO_2 is one of the best materials for making electrochemical biosensors. It is chemically stable, non-toxic, has a high surface-to-volume ratio of electrical conductivity and has strong electron transfer abilities. It has a diverse band gap (3.4 eV) as well as a higher isoelectric point (IEP) at around 9.2 [18], allowing to adsorb low IEP enzymes, for example, GO_x (glucose oxidase) without any further chemical treatment [19].

In this work, nanocomposite Co-doped CeO_2 was produced using the sol-gel process and the enzyme glucose oxidation (GOx) was adsorption on Co-doped CeO_2 without the need of a mediator. The sensing behaviour of Co-doped CeO_2 deposited on gold electrode as biosensor for glucose was investigated in terms of detection limit (K_m), sensitivity and response time.

EXPERIMENTAL

In this work, cerium(III) nitrate hexahydrate, $[Ce(NO_3)_3 \cdot 6H_2O]$, cobalt(II) nitrate hexahydrate $[Co(NO_3)_3 \cdot 6H_2O]$, citric acid, ethanol, potassium chloride, potassium ferricyanide, chitosan (SDFCL, India) and glucose oxidase (GOx) enzyme (*Aspergillus niger* Himedia, India) were used. For the preparation of solutions and buffers, deionized water was employed.

Preparation of Co-doped CeO_2 nanocomposite (CCO): The sol-gel citrate approach was used to prepare cobalt doped in CeO_2 (CCO) nanocomposites. To make a homogeneous mixture, the precursor cerium nitrate, cobalt nitrate (5, 10 and 15% by weight) and citric acid were mechanically grounded (mechanical process) for 0.5 h using a mortar pestle. Ethanol solution (50 mL) was added with the fine powder in order to get a homogenous solution and shaked it continuously for 3 h at 80 ºC on a magnetic stirrer. This solution was then heated in a heating chamber at about 130 ºC for 12 h to generate a gel precursor. The resulting gel precursor was calcined for 3 h at 350 ºC in a muffle furnace. For around 6 h, the dry powder were again 450, 550, 650 ºC (Fig. 1). Table-1 displays the nanoparticles that were created.

Preparation of CHIT/CCO/Au electrode: The gold plate was frequently washed with ethyl alcohol then rinsed with de-
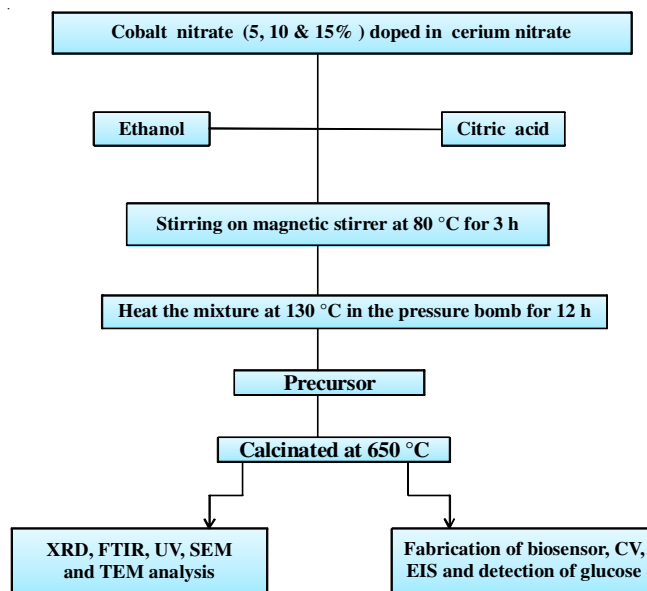
Fig. 1. Synthetic route of Co doped CeO_2 nanocomposite

ionized water. To make a Co-doped CeO_2 (CCO) modified gold electrode. Chitosan (10 mg), an organic copolymer, with 10 mg sol-gel formed Co-doped CeO_2 (CCO) (1:1) was combined in 100 mL of 0.2 M acetic acid and agitated at room temperature 3 h. Ultimately, a sticky chitosan-nano Co-doped CeO_2 (CCO) solution was created. Pour the suspension evenly over a previously washed gold plate using the spin coating method until a suitable layer was coated and dried at room temperature. A dry CHIT/CCO/Au electrode was rinsed with a 50 mM phosphate buffer solution many times.

Immobilization of glucose oxidase enzyme and fabrication of biosensor: For enzyme bioelectrode, a solution of glucose oxidase (GOx) was first prepared in 0.1 mol PBS (pH 7.0). The mixture was mixed and 5.0 mL of resulting solution was pipette out onto the surface of a pre-treated CHIT/CCO/Au electrode using the physical adsorption technique. Finally, the enzyme electrode (GOx/CHIT/CCO/Au) was submerged in 0.1 mol PBS (value of pH 7.0) to clean an electrode surface of a non-immobilized enzyme. When not in use, the enzyme bioelectrode was kept at 4 ºC.

Characterization: It was done with an X-ray diffractometer that used CuKα emission ($\lambda = 0.15418$ nm) to examine the phase purification of the nanocomposite made from Co-doped CeO_2 (CCO). It was done in the range of 20º to 80º (2θ). Fourier transforms infrared (FTIR) spectrophotometer (Shimadzu IR affinity-1, Japan) to examine the nanocomposite even more. This study was observed for the nanocomposite the nanocomposite between 400 and 4000 cm^{-1}, and UV-visible measurement was used to evaluate their optical properties (Shimadzu-

TABLE-1 SYNTHESIZED NANOPARTICLES WITH STOICHIOMETRIC RATIO OF PRECURSOR			
Nanoparticles	Cerium nitrate	Dopant cobalt nitrate	Calcinations
CeO_2	0.1 mol	Nil	450°, 550°, 650°
5% Co doped CeO_2 (CCO)	0.1 mol	1.455 g	450°, 550°, 650°
10% Co doped CeO_2 (CCO)	0.1 mol	2.910 g	450°, 550°, 650°
15% Co doped CeO_2 (CCO)	0.1 mol	4.365 g	450°, 550°, 650°

1800, Japan) (Shimadzu-1800, Japan). The morphology of a Co-doped CeO₂ nanocomposite was investigated using scanning electron microscopy (SEM) on a Nova Nano SEM-450 and transmission electron microscopy (TEM) on a Philips technical-20. Electrochemical glucose sensing has been done on a CH instrument (Electrochemical analyzer, USA) with a three-electrode compartment. The reference electrode madeup of Ag/AgCl, platinum (Pt) wire was used as an auxiliary electrode and a CHIT/Co doped CeO₂(CCO)/Au working electrode is used in PBS solution containing 5 M [Fe(CN)₆]$^{3-/4-}$.

RESULTS AND DISCUSSION

X-ray diffraction studies: X-ray diffraction (XRD) pattern was recorded to analyze the crystalline phase and pureness of the produced materials. Fig. 2 depicts the XRD pattern of synthesized 15% Co-doped CeO₂ (CCO) nanoparticles. The diffraction peaks are located along the planes (111), (200), (220), (311), (222), (400), (331) and (420), with Bragg's angles of 29.0º, 33.0º, 47.0º, 56.0º, 59.0º, 69.0º, 76.0º and 79.27º, respectively. Reflection of the face-centered cubic fluorite arrangement of 15% Co doped CeO₂ is shown. It is in line with the JCPDS PDF (Card No. 34-0394). The XRD spectra show confirm peaks suggesting that the produced product is crystalline. There is no impurity peak, such as other kinds of ceric oxides.
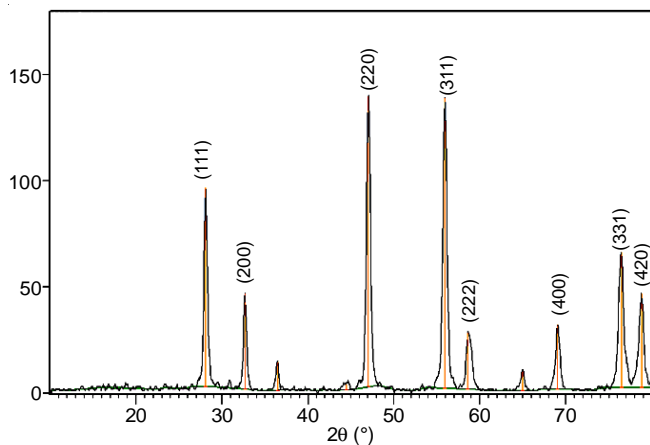
Fig. 2. XRD spectra of 15% Co doped in CeO₂

The average crystalline size calculated *via* the Debye Scherrer formula:

$$D = \frac{K\lambda}{\beta \cos\theta} \qquad (1)$$

where K denotes the shape factor with a range of 0.90, λ is the wavelength of the X-rays employed, β indicates the full width at half maxima of the corresponding peaks. The calculated grain size calculated from the highest intensity peak at (220) at Bragg angle 47.0º was 18.4 nm with lattice strain 0.0049 nm. (From Table-2) These findings suggest that the crystalline size of 15% Co-doped CeO₂ nanoparticles is affected by the amount of Co-doped and the annealing temperature. Doping prevents the formation of crystalline CeO₂ grains. The lattice parameter reduction is due to the lesser ionic radius of dopant

Co^{2+} (0.79 Å) as associated with Ce^{4+} (0.97 Å). Arul *et al*. [20] reported the crystallite size for Co-doped CeO₂ nanoparticles, was estimated from the intercept and determined to be 8.83 and 15.75 nm, respectively. Moreover, the particle size of the nanoparticles (CCO) is in perfect accord with the TEM image.

TABLE-2
SUMMARY OF CRYSTALLINE SIZE AND FWHM

Nanoparticles	2θ (°)	FWHM [2θ (°)]	Particle size (nm)
CeO₂ NPs	28.2	0.251	30.65
15% Co doped CeO₂	47.0	0.4920	18.4

UV-Visible studies: The UV-visible spectrum is presented in Fig. 3, where 15% Co-doped CeO₂ (CCO) nanoparticles display the well-defined high absorbance peak at 422 nm. All other peaks are between 200 and 400 nm. The absorption data with the direct transition yields the bandgap energy (E$_g$) (eqn. 2).

$$\alpha h\nu = A(h\nu - E_g)1/2 \qquad (2)$$

where α denotes the optical absorption coefficient, h represents the photon energy, E$_g$ indicates the direct band gap and A is the constant. The bandgap value of 15% Co-doped CeO₂ (CCO) was determined to be 2.93 eV lower in this study compare with pure CeO₂ nanoparticles reported in the literature. Pokha *et al*. [21] described the direct bandgap value compared from 3.56 eV to 3.71 eV for CeO₂ nanoparticles synthesized by sol-gel utilizing egg white. The reduction in bandgap energy for Co-doped CeO₂ relative to pure CeO₂ is due to the formation of trapping levels between the conduction and valence bands of CeO₂ [22,23].
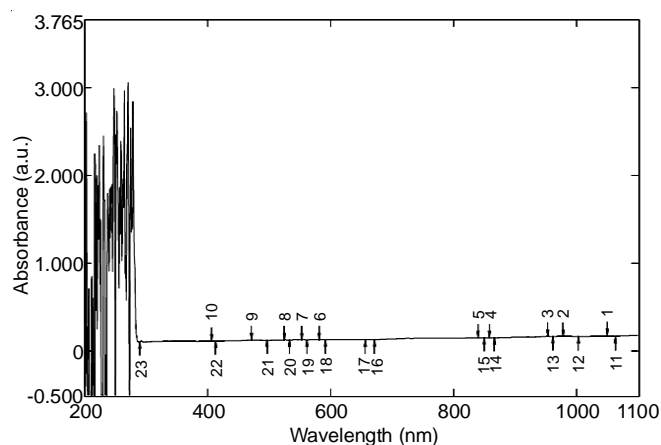
Fig. 3. UV-Visible spectra of 15% Co doped CeO₂ (CCO)

FTIR studies: FTIR experiments were investigated using the KBr pellet method to investigate the chemical structure of Co-doped CeO₂ nanoparticles. There were well-defined absorption maxima at 451.34, 540.07, 628.79, 1616.35 and 3433.29 cm^{-1} (Fig. 4). The shrill and extreme absorption peak at 451.34 cm^{-1} corresponds to symmetric bending of O-Ce-O, while the other two absorption peak bands at 540.07 and 628.79 cm^{-1} are due to asymmetric bending of O-Ce-O. Correspondingly,
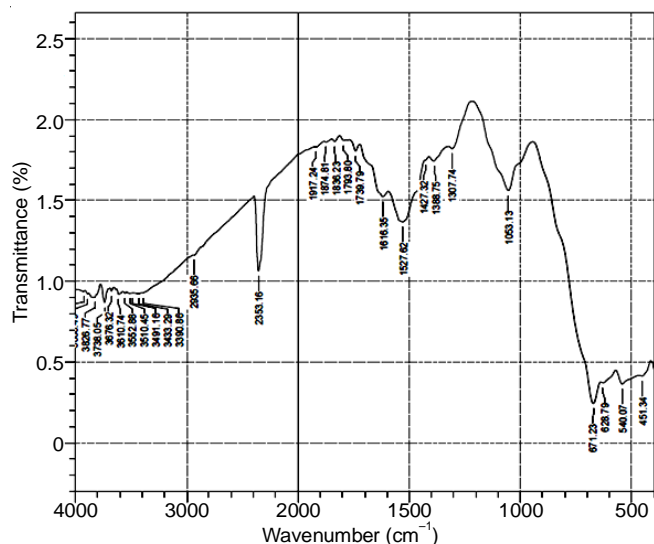
Fig. 4. FTIR spectra of 15% Co doped CeO₂ nanocomposite

SEM studies: Fig. 5 showed the morphological characteristics of the synthesized samples. The SEM pictures of 15% Co-doped in CeO_2(CCO) revealed that the synthesized material contains nanosized particles, which are cultivated in very dense populations. Nanodisperses and spherical ceramics like particles agglomerate to form the nanocomposite. Furthermore, the nanoparticles were homogenous and agglomerated by tiny nanoparticles.

TEM studies: The surface morphology of 15% Co doped CeO_2 nanocrystals was examined using TEM, which indicate the spherical nanocrystals evenly produced and agglomerated together like clusters. The grain size distribution with the most nanoparticles ranging from 17.92 to 21.83 nm (Fig. 6). Surface modification restricts the crystal development and inhibits aggregation during nanoparticle production owing to steric repulsion among the particles [24,25]. Furthermore, the mean grain size is quite near the average crystallite of XRD pattern particles.

Electrochemical impedance spectroscopy (EIS): A semicircle and a linear portion are included in the usual impedance spectrum. The arc diameter correlates to an electron transfer resistance (RCT) at higher frequencies, whereas the linear part corresponds to the diffusion-restricted process at lower frequencies. A CHIT/CCO/Au electrode was placed in 5.0 mM

the significant absorption peaks at 1616.35 cm⁻¹ and 3433.29 cm⁻¹ may be attributed to H_2O bending vibration modes and surface O-H broadening modes. It is attributable due to water molecule adsorption on the surface of the nanocomposite.
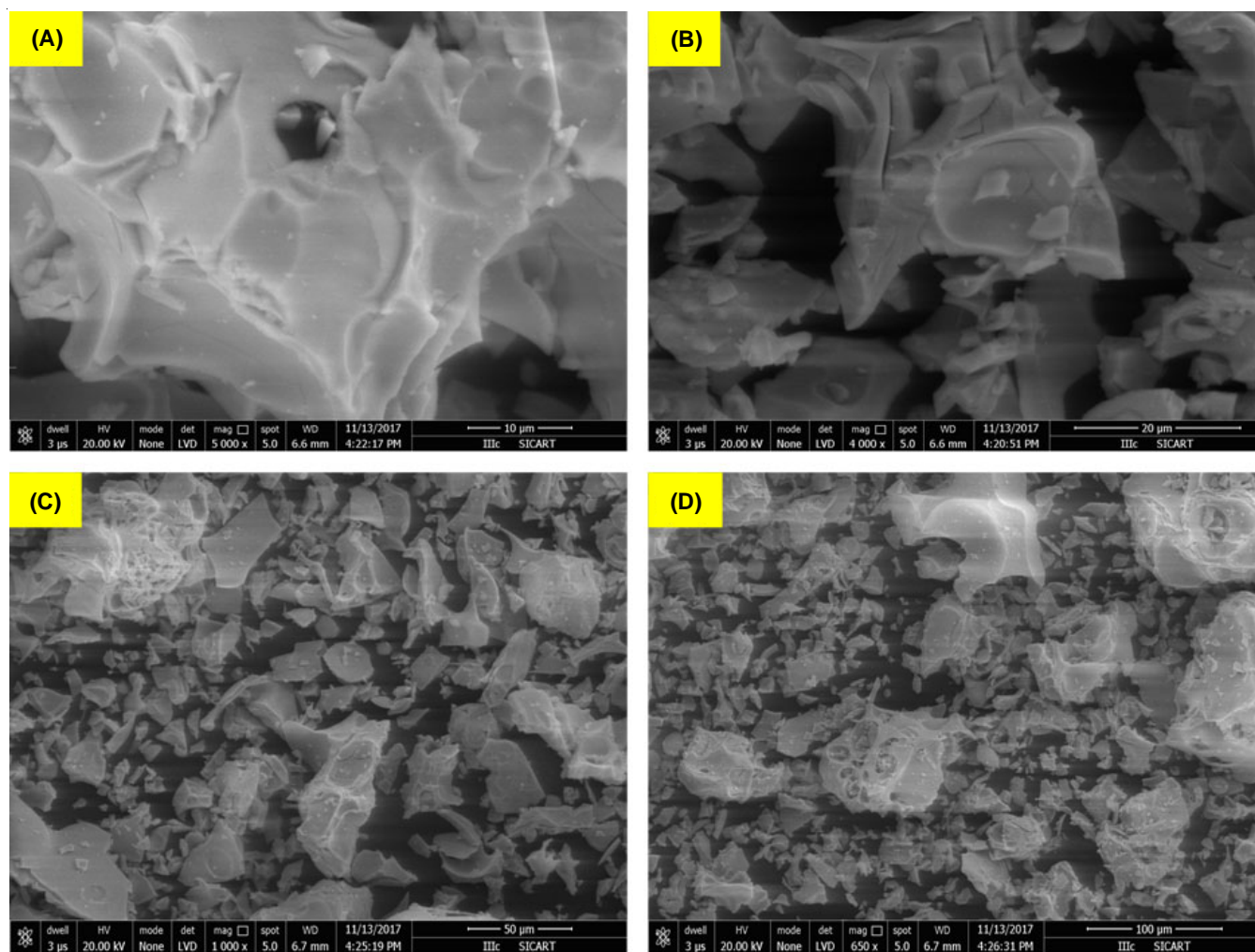
Fig. 5. (A&B) Low magnification, (C&D) high magnification, SEM micrograph of 15% Co doped CeO₂ nanoparticles
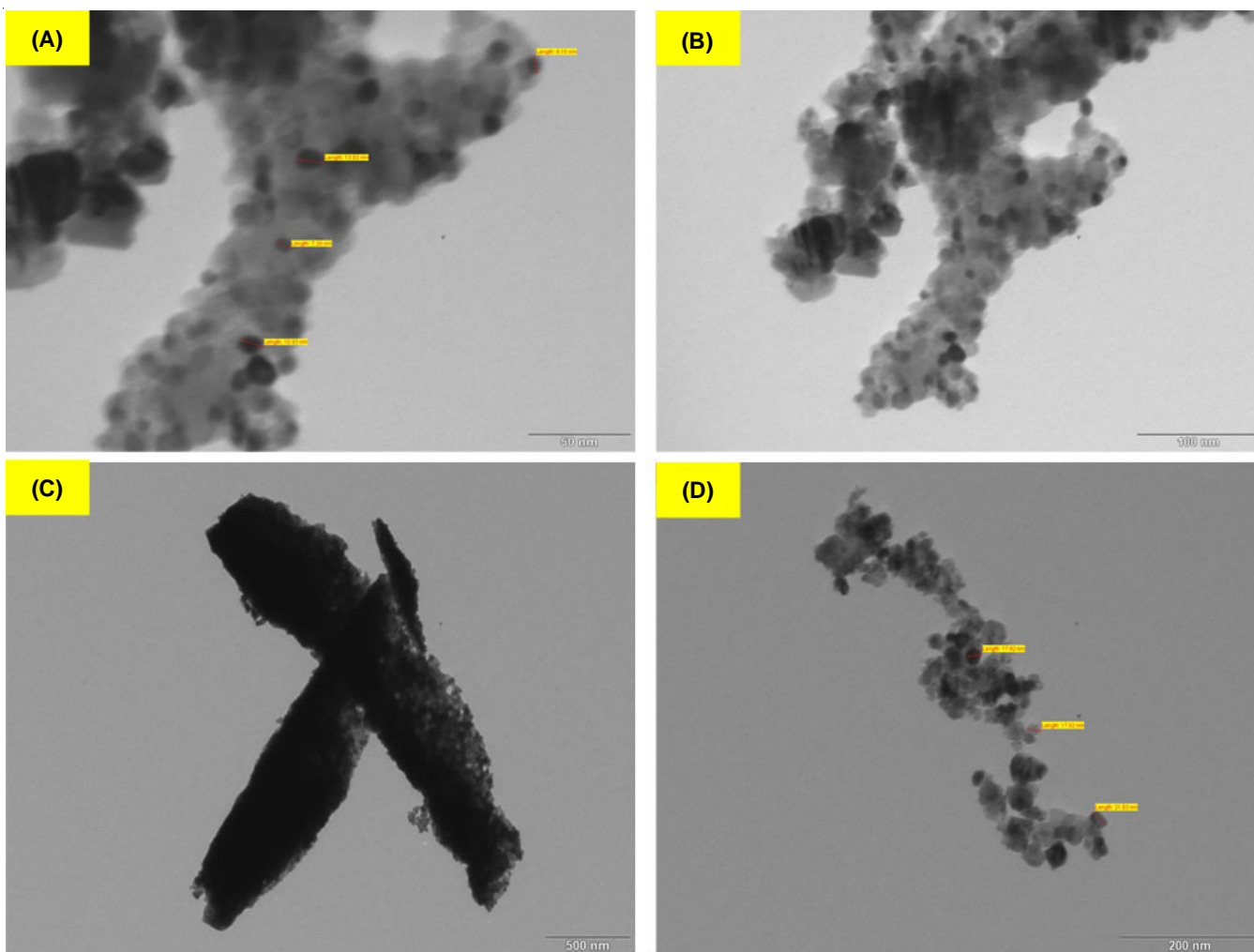
Fig. 6. (A&B) Low magnification, (C&D) high resolution, TEM micrograph of 15% Co doped CeO$_2$ nanoparticles

[Fe(CN)$_6$]$^{3-/4-}$ with 0.1 M KCl and an EIS measurement was performed. The frequency ranged from 10 to 10^5 Hz, and the amplitude was 0.005 V. Fig. 7 shows that the RCT value for GOx/CHIT/CCO/Au bioelectrode grows considerably from 13 to 33 Ω indicating that the GOx enzyme has been effectively immobilized.
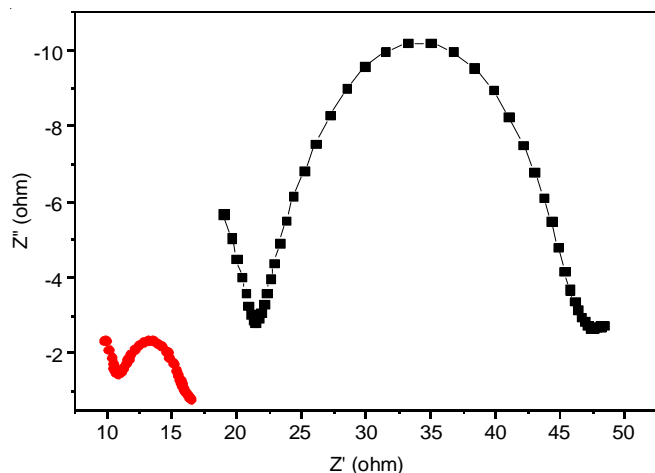
Fig. 7. EIS of (a) CHIT/CCO/Au electrode (b) GOx/CHIT/CCO/Au bioelectrode

Cyclic voltammetry studies: The cyclic voltammogram graph was obtained by plotting potential at the working electrode *vs.* applied voltage (*i.e.* the working electrode's potential). In a typical CV experiment, a cell is outfitted with three electrodes: a reference electrode, a working electrode and a counter electrode. This arrangement is commonly referred to as a three-electrode arrangement, by Ag/AgCl acting as the reference electrode and platinum serving as the counter electrode. The CV investigation in this instance was carried out in a three-electrode cell arrangement using GOx/CHIT/CCO/Au (as working electrode), Pt wire (as counter) and Ag/AgCl (as reference). The cyclic voltammetry (CV) was achieved within the voltage range of -10 mV to 600 mV and a scan rate of 10 mV s^{-1}.

Figs. 8a-c show the cathodic currents of 0.009, 0.004, and 0.003 Å for bare Au electrodes, CHIT-nano CCO/Au electrodes and GOx/CHIT-nano Co-doped CeO$_2$/Au bioelectrodes, respectively. After CHIT-nano CCO formation on the gold electrode, the peak current on the cathode drops. It suggests that the semiconducting Co-doped CeO$_2$ layer limits the conductive sites while still allowing electrochemistry to happen at the electrode. Furthermore, the conducting nature of Co-doped CeO$_2$ nanoparticles, as well as the creation of a circuit between the positively charged Co-doped CeO$_2$ nanocrystals
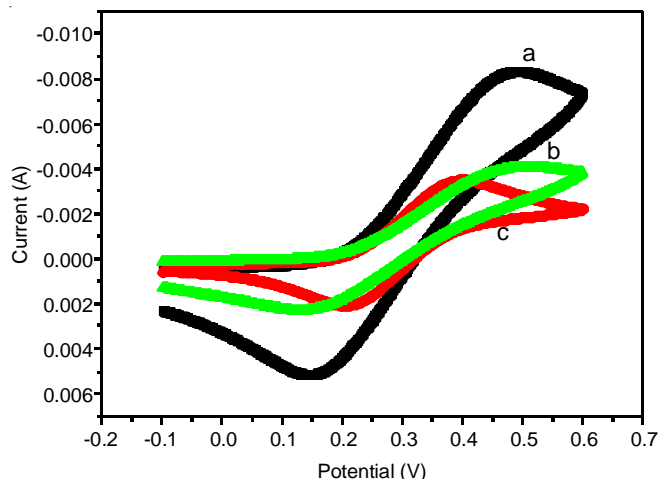
Fig. 8. CVs of (a) Bare Au electrode (b) CHIT/CCO/Au electrode (c) GOx/CHIT/CCO/Au bioelectrode

and the hydroxylamine group of chitosan, were observed. The current amplitude was lower after the glucosidase enzyme was immobilized on the CCO nanoparticles. The enzyme is non-conductive, making it difficult for electrons to move through the PBS electrolyte because of ferro/ferri molecules. Furthermore, the redox capacity and peak-to-peak separation (ΔE_p) of the GOx/CHIT/CCO/Au bioelectrode increase. It was ascribed to the enzyme's poor electrical conductivity and the low electrical conductivity of the CHIT/CCO/Au electrode.

Electrochemical response of GOx/CHIT/Co-doped CeO₂/Au bioelectrode: Fig. 9a depicts the CV investigations of a GOx/CHIT-CCO/Au bioelectrode with varying concentrations of glucose (50-250 mM) added while submerging its electrolyte into KCl (0.1M) contained $[Fe(CN)_6]^{3-/4-}$. A linear rise in peak current with increasing analyte concentration suggests an increase in charge transport to the working electrode. Fig. 9b depicts the calibration curve from which glucose detection may be calculated. The bioelectrode exhibits two linear ranges, 50-160 mM and 160-220 mM, with a sensitivity of 13.5A mM⁻¹ cm². Sensitivity was calculated as the proportion of the calibrating curve's slope to the effective surface area of the working Au electrode. Sensitivity can be calculated by eqn. 3:
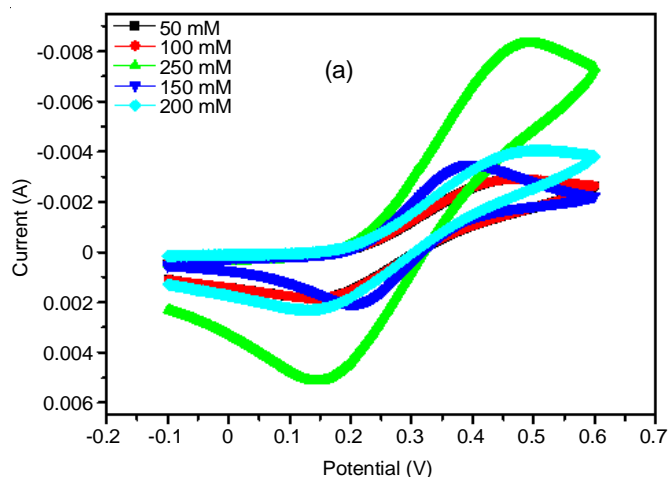
$$Sensitivity = \frac{Slope\ of\ the\ calibration\ curve}{Active\ surface\ area\ of\ the\ working\ electrode\ Au} \quad (3)$$

In both cathodic and anodic current, the lower limit of detection (30 mM) with linear regression coefficient (R^2) was determined to be 0.999. In electrocatalytic oxidation of glucose, a bioelectrode might work like this:

$$C_6H_{12}O_6 + O_2 + H_2O \xrightarrow{\ GOx\ } C_6H_{12}O_7 + H_2O_2$$

$$H_2O_2 + 2H^+ + 2e^- \xrightarrow{\ cco\ } 2H_2O$$
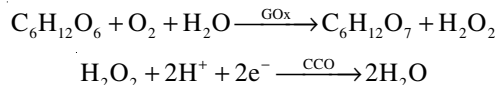
Effect of potential scan rate: The CV measurements were took on a GOx/CHIT/CCO/Au bioelectrode due to (scan rate), which ranged from 10 to 100 mV/s. Fig. 10a depicts the intensities of anodic (IPC) peak currents and the increasing energy shift, which rises continuously with the square root of the scanning speed ($v^{½}$), demonstrating the process to be a diffusion-controlled electron-transfer mechanism.

Determination of Michaelis-Menten constant (K_m): In general, the perceived Michaelis-Menten constant (K_m) is being used to assess the biological processes of an immobilized enzyme. It may be determined using the Lineweaver-Burke formula [26] as shown in eqn. 4:

$$\frac{1}{I_{ss}} = \frac{K_m A_{pp}}{I_{max}} \frac{1}{C} + \frac{1}{I_{max}} \quad (4)$$

where I_{ss} is indeed the steady-state current following substrate addition, C is the substrate bulk concentration, and I_{max} is indeed the maximum current recorded under saturating substrate conditions. Fig. 10b depicts a double reciprocal plot of anodic peak current *vs.* concentration of the analyte (glucose). The slope of a graph may be used to compute the value of (K_m). The amount of K_m, which reflects enzymatic affinity, is found to be 3.010 mM. The smaller the value of K_m in comparison to glucose oxidase (GOx) enzymes implies that the substrates and product molecules may quickly move to and from the CHIT/Co-doped CeO₂ matrix. The smaller value of K_m reported in the current studies with glucose samples (Table-3) illustrates the benefit of the nanoporous CeO₂ matrix over other oxides. Another reason why cobalt-doped CeO₂ is better than other oxides or polymer matrices for enzyme immobilization is
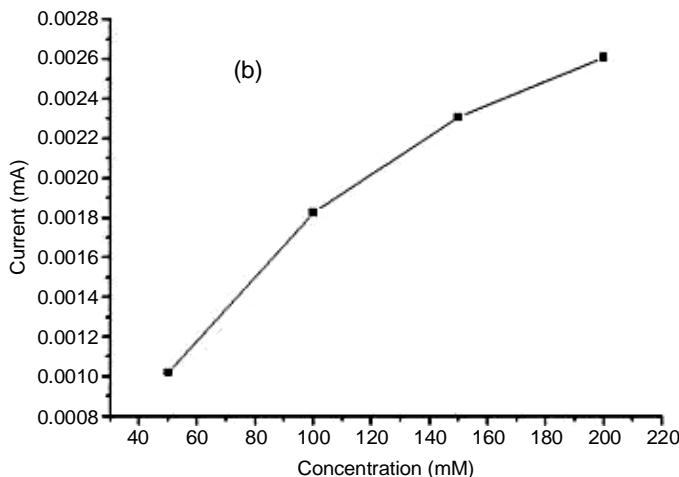
Fig. 9. (a) CVs of biosensors at different concentration of glucose at scan rate 10 mV s⁻¹ (b) calibration plot
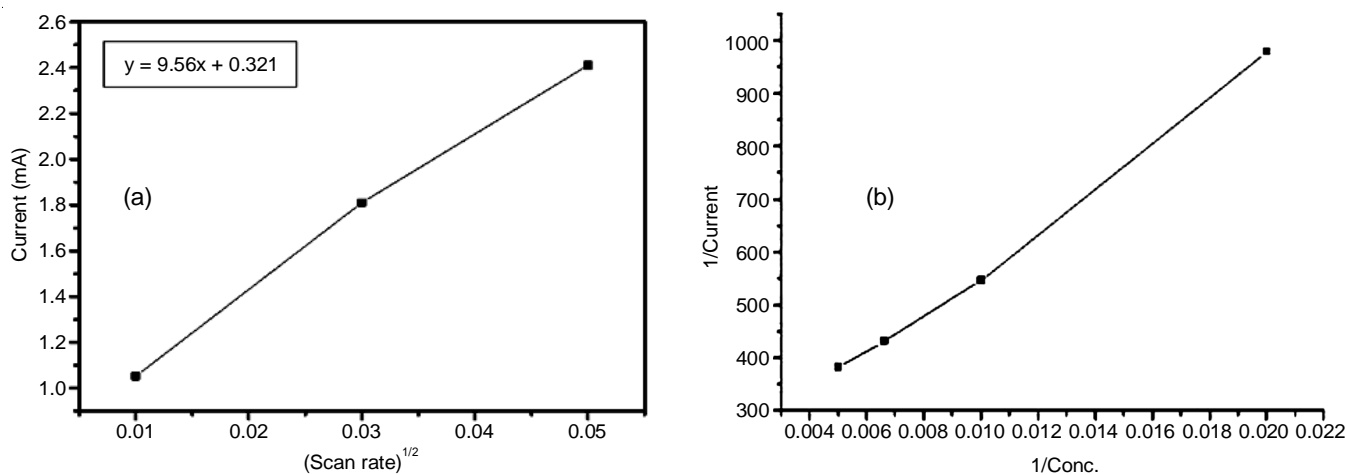
Fig. 10. (a) Plot of anodic peak current *vs.* $v^{1/2}$ (b) line weaver Bruke plot

TABLE-3
COMPARISON OF THE GOx/CHIT/CCO/Au BIO-ELECTRODE WITH OTHER MATRICES

Immobilization matrix	Method of immobilization	Linearity (mM)	K (mM)	Shell life	Ref.
ZnO nanorods	Physical	0.01-3.45	2.9	–	[29]
CeO₂	Physical	1.39-8.33	1.01	10 weeks	[30]
Gold nanoparticles	Covalent	15	3.74	6 months	[31]
Co doped CeO₂ (CCO)	Physical	50-160	3.010	28 days	Present work

because Ce^{3+}/Ce^{4+} redox pairs make it easy to transfer electrons and make good complexes with enzymes easier for enzymes to be attached. Because of this, the matrix has a nanostructure. It allows for reliable electron transmission between the enzyme's active site and the electrode and a large specific surface area that offers a suitable milieu for successful enzyme immobilization on the matrix's surfaces.

Furthermore, most biosensor matrices need crosslinkers for enzyme immobilization. It is not required for the oxide matrices utilized in this work because their large IEP makes it appropriate for mechanical immobilization. The significant value of K_m was reported to be comparatively 1.01 mM for immobilized GOx on CeO_2 nanoparticles and determined by a variety of factors like matrix and method of immobilization of enzymes, which could result in different complex formation in the specific enzymes as enzyme reactions are environmentally responsive.

Stability and reproducibility: The primary prerequisite of any biosensor is stability. It was kept in de-ionized water at 4 ℃ for 28 days. After 28 days, the GOx/CHIT/CCO/Au bioelectrode preserved 80.3% of its initial current response.

Conclusion

The Co-doped CeO_2 (CCO) nanoparticles were produced using the sol-gel technique in this study. At 650 ℃, the XRD measurements show a face-centered cubic fluorite structure of 15% Co-doped CeO_2 (CCO) nanocomposite. The crystalline size was reduced from 30 to 18.4 nm. With the help of UV-visible spectra, it was estimated that the bandgap energy was 2.93 eV. It was smaller than the amount of pure CeO_2 nanoparticles. Furthermore, the glucose biosensor was created by physically adsorbing the glucose oxidase enzyme (GOx) onto

a CHIT/CCO/Au electrode. The constructed biosensor has shown excellent performance in terms of affinity, broad linear range (50-220 mM), low detection limit (30 mM), sensitivity 13.5 A mM⁻¹ cm⁻² and a low Michaelis-Menten constant (K_m = 3.010 mM), indicating that glucose oxidase enzyme has a high affinity for nanocomposite.

CONFLICT OF INTEREST

The authors declare that there is no conflict of interests regarding the publication of this article.

REFERENCES

1. I. Khan, K. Saeed and I. Khan, *Arab. J. Chem.*, **12**, 908 (2019);
   https://doi.org/10.1016/j.arabjc.2017.05.011
2. M. Nyoka, Y.E. Choonara, P. Kumar, P.P.D. Kondiah and V. Pillay, *Nanomaterials*, **10**, 242 (2020);
   https://doi.org/10.3390/nano10020242
3. C. Sun, H. Li and L. Chen, *Energy Environ. Sci.*, **5**, 8475 (2012).
   https://doi.org/10.1039/c2ee22310d
4. M. Coduri, S. Checchia, M. Longhi, D. Ceresoli and M. Scavini, *Front Chem.*, **6**, 526 (2018);
   https://doi.org/10.3389/fchem.2018.00526
5. A. Kumar, M. Kumari, M. Kumar, S. Kumar and D. Kumar, *AIP Conf. Proceed.*, **1728**, 020444 (2016);
   https://doi.org/10.1063/1.4946495
6. M. Ibrahim, Y. Temerk and H. Ibrahim, *RSC Adv.*, **7**, 32357 (2017);
   https://doi.org/10.1039/C7RA04331G
7. Z. Liu, Q. Wang, J. Wu, H. Zhang, Y. Liu, T. Zhang, H. Tian and S. Zeng, *ACS Appl. Mater. Interfaces*, **13**, 35804 (2021);
   https://doi.org/10.1021/acsami.1c09332
8. G. Mu, Y. Zeng, Y. Zheng, Y. Cao, F. Liu, S. Liang, Y. Zhan and L. Jiang, *Green Energy & Environ.*, (2021);
   https://doi.org/10.1016/j.gee.2021.11.001
9. B. Vodungbo, Y. Zheng, F. Vidal, D. Demaille, V.H. Etgens and D.H. Mosca, *Appl. Phys. Lett.*, **90**, 062510 (2007);
   https://doi.org/10.1063/1.2472520

10. J. Xie, H. Ping, T. Tan, L. Lei, H. Xie, X. Yang and Z. Fu, *Prog. Mater. Sci.*, **105**, 100571 (2019);
https://doi.org/10.1016/j.pmatsci.2019.05.004

11. S. Tang, Z. Dong, X. Ke, J. Luo and J. Li, *Int. J. Oral Sci.*, **13**, 42 (2021);
https://doi.org/10.1038/s41368-021-00147-z

12. Y. Chen, Y. Feng, J.G. Deveaux, M.A. Masoud, F.S. Chandra, H. Chen and L. Feng, *Minerals*, **9**, 68 (2019);
https://doi.org/10.3390/min9020068

13. D. Hu, Q. Ren, Z. Li and L. Zhang, *Molecules*, **25**, 4785 (2020);
https://doi.org/10.3390/molecules25204785

14. M.A. Rahman, J. Halfar, W.H. Adey, M. Nash, C. Paulo and M. Dittrich, *Sci. Rep.*, **9**, 11869 (2019);
https://doi.org/10.1038/s41598-019-47785-2

15. N. Butto, N. Cotrina Vera, F. Díaz-Soler, M. Yazdani-Pedram and A. Neira-Carrillo, *Crystal*, **10**, 453 (2020);
https://doi.org/10.3390/cryst10060453

16. N.H. Bansod, G.N. Chaudhari and S.D. Patil, *Der Pharma Chem.*, **5**, 144 (2013).

17. N.H. Bansod, *Eur. J. Biomed. Pharm. Sci.*, **7**, 273 (2020).

18. G.N. Chaudhari, N.H. Bansod and A.B. Bodade, *Int. J. Curr. Eng. Scient. Res.*, **6**, 1401 (2019).

19. N.H. Bansod, A.B. Bodade and G.N. Chaudhari, *Eur. J. Biomed. Pharm. Sci.*, **4**, 732 (2017).

20. N.S. Arul, D. Mangalaraj, R. Ramachandran, A.N. Grace and J. Han, *J. Mater. Chem. A Mater. Energy Sustain.*, **3**, 15248 (2015);
https://doi.org/10.1039/C5TA02630J

21. S. Phokha, S. Pinitsoontorn, P. Chirawatkul, Y. Poo-arporn and S. Maensiri, *Nanoscale Res. Lett.*, **7**, 425 (2012);
https://doi.org/10.1186/1556-276X-7-425

22. P.P. Ortega, B. Hangai, H. Moreno, L.S.R. Rocha, M.A. Ramírez, M.A. Ponce, E. Longo and A.Z. Simões, *J. Alloys Compd.*, **888**, 161517 (2021);
https://doi.org/10.1016/j.jallcom.2021.161517

23. M.E. Khan, M.M. Khan and M.H. Cho, *Sci. Rep.*, **7**, 5928 (2017);
https://doi.org/10.1038/s41598-017-06139-6

24. P. Tamizhdurai, S. Sakthinathan, S.M. Chen, K. Shanthi, S. Sivasanker and P. Sangeetha, *Sci. Rep.*, **7**, 46372 (2017);
https://doi.org/10.1038/srep46372

25. M.B. Gawande, A. Goswami F.Z. Felpin, T. Asefa, X. Huang, R. Silva, X. Zuo, R. Zboril and R.S Verma, *Chem. Rev.*, **116**, 3722 (2016);
https://doi.org/10.1021/acs.chemrev.5b00482

26. T.T.N. Anh, V.V. Thu, H.S. Dang, V.H. Pham and P.D. Tam, *Adv. Polym. Technol.*, **2021**, 6627645 (2021);
https://doi.org/10.1155/2021/6627645